

Characterization and Analysis of Plastic Instability in an Ultrafine-Grained Medium Mn TRIP Steel

Zhenjie Teng,* Haoran Wu, Sudipta Pramanik, Kay-Peter Hoyer, Mirko Schaper, Hanlong Zhang, Christian Boller, and Peter Starke

Herein, the mechanical and magnetic behavior of an ultrafine-grained (UFG) medium manganese (Mn) transformation-induced plasticity (TRIP) steel is focused on in its plastic instability. The in situ methods of digital image correlation (DIC) and magnetic Barkhausen noise (MBN) are used to macroscopically characterize the propagation of the Lüders band (stretcher–strain marks) and the evolution of MBN activities during quasistatic tensile deformation. The evolution of microstructure during the plastic instability is investigated ex situ using X-Ray diffraction (XRD) and transmission electron microscopy (TEM) for selected plastic strain states. It is showed in the results that the plastic instability of this steel is associated with an increase of hardness and enrichment of dislocation density, which can also amplify the MBN signal, while the derived coercivity behaves reversely on an overall trend due to work hardening. The different stress response of the medium Mn steel is closely related to the kinetic martensite microstructure, which in turn modifies the domain–structure response. Thus, the MBN can be used as a potential means for nondestructive evaluation (NDE) for the strengthening of the UFG medium Mn TRIP steel.

1. Introduction

The increasing demand for crashworthiness–improvement and weight reduction in the automotive and other transportations vehicles has led to the development of the third generation of advanced high-strength steels (AHSSs).^[1,2] Moreover, long-term use of lightweight steels can lead to a reduction in fuel consumption and thus detrimental emissions, contributing to carbon-neutrality targets in the longer term. Among those steels, the ultrafine-grained (UFG) medium Mn (3–12 wt%) transformation-induced plasticity (TRIP) steels, containing retained γ -austenite islands or films dispersed in an α -ferrite or α' -martensite matrix, emerge a great potential to be a strong candidate due to its excellent strength, ductility, and toughness performance.^[3]


The TRIP effect leads to big advantages with respect to forming processes, being specifically relevant for automotive application. On the one hand, this includes hardening due to martensitic transformation and higher stiffness due to the forming of profiles on the other. The TRIP effect normally appears at higher strains during the tensile loading, where retained γ -austenite present in the medium Mn steel transforms to α' -martensite resulting in high strength and elongation since the metastable austenite structure has higher ductility and a better ability to accommodate plastic strain. However, a discontinuous yielding phenomenon is the main drawback in such steels,^[4] which is to be observed from the yield point, followed by a stress plateau in the tensile stress–strain curve, where the Lüders band normally forms and propagates in such a stage. As a kind of plastic instability or localized deformation behavior, the Lüders band, which occurs in the tensile test, is not desired in cases such as for automotive application, as such a behavior can deteriorate the surface quality of the material and result in an unexpected weakening of the material's structural stability and even premature failure in some cases.^[5] Hence, such a plastic instability problem was investigated previously by a considerable number of studies with different characterization methods, for example, in situ measurements including digital image correlation (DIC),^[5–7] neutron diffraction,^[8,9] infrared thermography (IRT),^[5,6] and ex situ methods like electron backscatter diffraction (EBSD),^[10,11] X-Ray diffraction (XRD),^[12,13] as well as transmission electron

Z. Teng, H. Wu, C. Boller
Chair of Non-Destructive Testing and Quality Assurance
Saarland University
66125 Saarbrücken, Germany
E-mail: zhenjie.teng@hs-kl.de

Z. Teng, H. Wu, P. Starke
Department of Materials Science and Materials Testing
University of Applied Sciences Kaiserslautern
Kaiserslautern 67659, Germany

S. Pramanik, K.-P. Hoyer, M. Schaper
Chair of Materials Science
Paderborn University
Paderborn 33100, Germany

H. Zhang
Baoshan Iron and Steel Co., Ltd. & The State Key Laboratory of
Development and Application Technology of Automotive Steels (Baosteel)
Shanghai 201900, China

 The ORCID identification number(s) for the author(s) of this article can be found under <https://doi.org/10.1002/adem.202200022>.

© 2022 The Authors. Advanced Engineering Materials published by Wiley-VCH GmbH. This is an open access article under the terms of the Creative Commons Attribution-NonCommercial-NoDerivs License, which permits use and distribution in any medium, provided the original work is properly cited, the use is non-commercial and no modifications or adaptations are made.

DOI: 10.1002/adem.202200022

microscopy (TEM).^[14–16] Moreover, the underlying mechanisms for the plastic instability of medium Mn steel can be referred from the review literature.^[17,18] Nowadays, nondestructive testing (NDT) is in huge demand due to its enhanced capabilities for evaluating mechanical properties. With many of those techniques, the operation becomes increasingly intuitive, the measurement is noninvasive, and can even be contactless. Among the wide range of NDT techniques, magnetic Barkhausen noise (MBN) has been chosen to characterize the plastic instability/work hardening of the medium Mn TRIP steel analyzed along tensile tests to be presented here.

In contrast to ferromagnetic body-centered cubic (bcc) α -ferrite/body-centered-tetragonal (bct) α' -martensite, face-centered cubic (fcc) γ -austenite is paramagnetic. The cold-worked medium Mn TRIP steel therefore has detectable magnetic properties, which can be determined by MBN. MBN is emerged from the ferromagnetic materials through the discontinuous domain wall (DW) movements,^[19] which can be induced across a sample by applying a time-varying magnetic field. The MBN recorded in the form of an electrical voltage pulse, measured through applying a pickup coil or any similar sensing device located near the sample's surface. Furthermore, the MBN is strongly influenced by the types and numbers of pinning sites of the DWs within the material being tested, where the pinning sites act as barriers for the DW movement and are resulted of various microstructural defects, for example, voids, inclusions, phase transformations, grain boundaries, and dislocations.^[20,21] However, it is not easy to directly link the magnetic properties with the amount of deformation-induced martensite directly. The MBN is very sensitive to the microstructure and applied/residual stress. The lattice defects induced by strain hardening can temporarily pin the DWs, and the high internal stress, which is generated due to an incompatible phase transformation strain, can also affect the motion of the magnetic domain.^[22] The gradual deformation-induced martensite transformation will increase the work hardening of the medium Mn TRIP steel, and the fine martensite grains that generate inside the austenite grains will make the dislocation movement more difficult.^[23] Thus, monitoring the MBN properties can be helpful for the evaluation of the Lüders band formation or the deformation degree of medium Mn TRIP steel, even in the relatively early stages before the ultimate fracture, which seems to have been barely studied

and understood, as can be concluded from lack of literature so far.

What follows, details of the experiments are presented first, which includes the material information, test procedures of in situ DIC, MBN, and ex situ XRD as well as TEM. The MBN profile curves, dislocation densities, hardness, and phase content determined for selected strains are compared to find out what changes in microstructural, mechanical, and magnetic properties occur, where the Lüders propagation is then given and discussed systematically. The results are discussed systematically to draw final conclusions.

2. Experimental Section

An UFG medium Mn TRIP steel with a chemical composition of Fe–7Mn–0.14C–0.2Si (in wt%) was studied in the current investigation. The steel was cold-rolled and annealed, in which the material was heated at a rate of $5\text{ }^{\circ}\text{C s}^{-1}$ until $620 \pm 15\text{ }^{\circ}\text{C}$ was reached and then kept for 24 h in a nitrogen atmosphere protection. The intercritical annealing temperatures ranged from $593.7\text{ }^{\circ}\text{C}$ (A1) to $691.3\text{ }^{\circ}\text{C}$ (A3). After that, the steel was cooled down in air to room temperature. The microstructure consisted of two dominant phase contents: ferrite and retained austenite. The grain size of the annealed material was $\approx 360\text{ nm}$, and the overall γ -austenite had $\approx 34.7\%$ volume fraction measured by XRD. The inverse pole figure map and the phase map of the material were observed by EBSD as shown in **Figure 1**. The magnetic domain images of the annealed material could be visualized by using magneto-optical Kerr effect microscopy (MOKE). **Figure 2** shows the evolution of the intensity of the magnetic domain images at 4.96, 19.97, 35.01, and 40.01 mT, respectively, with the range of magnetic field from -170 to 170 mT .

In this investigation, a standard dog-bone-shaped specimen with a gauge dimension of $35 \times 6 \times 1.4\text{ mm}^3$ was designed and machined along the rolling direction (RD) from the annealed steel plate. The entire specimens' surfaces were polished to a mirror-like finish before uniaxial tensile tests were carried out with a universal tester (SHIMADZU AGS-X, 10 kN) and performed at a cross-head constant speed of 1 mm min^{-1} at room temperature.

The surfaces of the specimen were speckled patterned with white and black paints to obtain a better contrast for the DIC measurement. To evaluate the strain distribution, optical photos

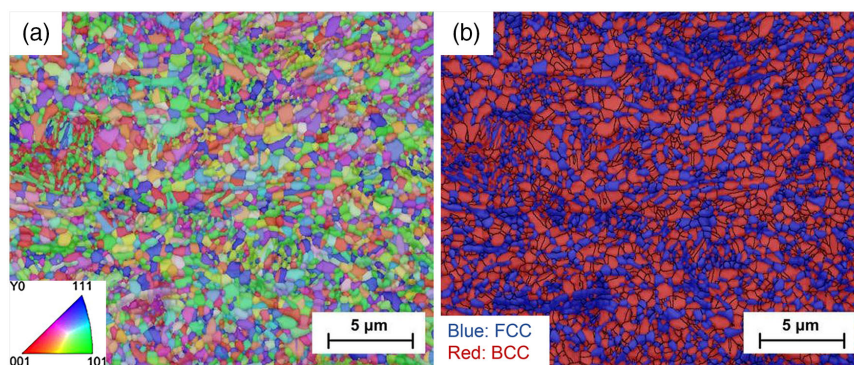


Figure 1. Crystallographic characteristics of the medium Mn transformation-induced plasticity (TRIP) steel: a) electron backscatter diffraction (EBSD) inverse pole figure map; b) EBSD phase map: ferrite and austenite are represented by red and blue color, respectively.

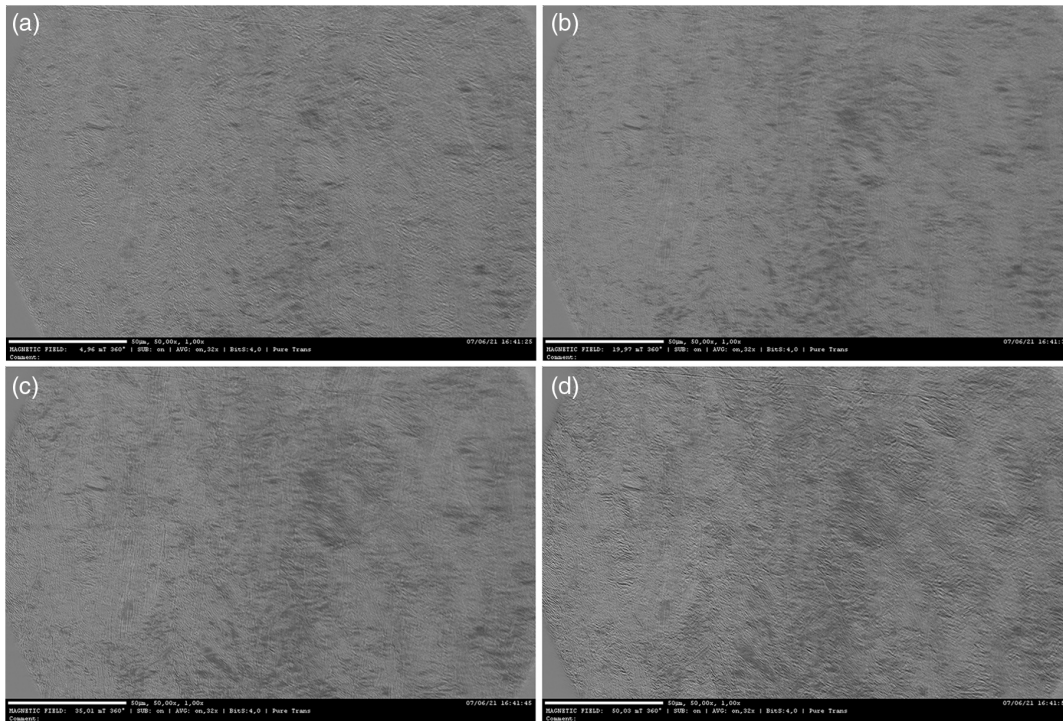


Figure 2. The evolution of the intensity of magnetic domain images by using a Kerr microscope at magnetic field of a) 4.96 mT; b) 19.97 mT; c) 35.01 mT; and d) 40.01 mT, respectively, of the medium Mn TRIP steel.

of such prepared sample surfaces were taken at a framerate of 1 fps during the test. The kinematic strain field measurement was performed by a Canon 6D Market II camera with an EF 100 mm f/2.8 L IS USM lens.

The MBN was investigated by using a μ magnetic measurement system of QASS. The sinusoidal magnetic signal was excited at a frequency of 10 Hz with a coil voltage amplitude of 955 mV. Each excitation lasted 500 ms (five cycles). The applied sensor was positioned with a minimal liftoff of ≈ 0.3 mm, perpendicularly to the surface of the specimen. The raw signal was processed by selecting a region of interest (ROI) within a frequency band of 120–500 Hz, while denoising of the signal was made in both frequency and time domain. To avoid phase shift, only envelope curves were extracted rather than using a smoothing algorithm. The MBN signal peaks (unitless) and their positions (in mV regarding the coil voltage) were determined and used to characterize the microstructural changes on the specimens. The peak positions are considered to be correlated with the coercivity.

Quantitative XRD measurements were performed to examine the distribution and transition of the phases for the selected strains of the tensile deformation using a Seifert XRD 3000 PTS diffractometer equipped with monochromatic Cr $K\alpha$ radiation ($\lambda = 2.2897 \text{ \AA}$) with a scanning range (2θ) of 35° – 160° . The voltage applied to the X-Ray tube was 40 kV with a current of 40 mA in a scanning step of 2θ of 0.01° . The measured area was located in the middle center of the interrupted samples, however, for the final fractured sample, it was measured close to the fracture surface.

For the TEM investigations, the samples from the gauge section after the interrupted tensile tests were thinned to a

thickness of $\approx 400 \mu\text{m}$ (Struers Secotom-5). The sides of the samples cut in RD to the transverse direction (TD) were polished to a thickness of $\approx 100 \mu\text{m}$ using abrasive papers. After that, disks with a diameter of 3 mm were punched from these samples. Electron transparent samples were prepared by twin jet electropolishing (Struers Tenupol-5). The electropolishing was conducted at 21 V, 18 mA, -21°C using a solution with 5% perchloric acid and methanol. TEM was performed with a JEOL JEM-ARM 200 F microscope operating at 200 kV acceleration voltage. For dislocation imaging, suitable tilting of the samples was undertaken in a double-tilt sample holder. The sample thickness was measured using the energy-filtered TEM (EFTEM) mode. During EFTEM operation images of the same region were taken 1) using a 10 eV energy filter placed on the zero-loss peak and 2) without an energy filter. For dislocation density calculation, equally spaced horizontal and vertical lines were drawn on the TEM images of samples taken at the same magnification. The intersection points of the lines with dislocations were counted. Subsequently, the dislocation density was calculated by $\rho = 2N/Lt$,^[24] where ρ is the dislocation density, N is the total intersection points, L is the total length of the horizontal and vertical lines, and t is the sample thickness.

3. Results and Discussion

3.1. Mechanical Behavior and Damage

Two exemplary tensile stress–strain curves obtained at room temperature of the medium Mn TRIP steel tests are illustrated

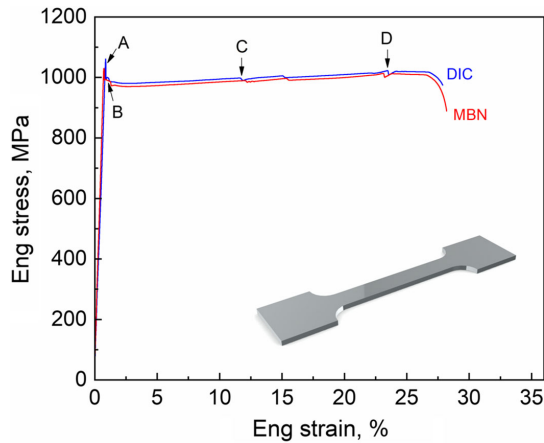


Figure 3. Engineering stress–strain curves of the medium Mn TRIP steel obtained by tensile tests at room temperature until the rupture; and schematic geometry of the tensile specimen as the inset.

in **Figure 3**. One of them was accompanied by DIC and the other by MBN measurement. The result shows a 0.2% offset stress of 1025 MPa, with total elongation of $\approx 28\%$. Such excellent strength–ductility trade-offs have been reported elsewhere for the medium Mn steels having UFG microstructures.^[8,25,26] Furthermore, this behavior is contributed from the deformation-induced $\gamma \rightarrow \alpha'$ -martensitic transformation, where significant grain refinement and a high strain-hardening rate occur.^[27]

The material shows an elastoplastic behavior, after reaching the upper-yield point. Here, the stress rapidly decreases from 1060 to 985 MPa (from point A to B) when strain is increased, with a small step in between, before this stress becomes a nearly constant value until a strain of 11.8% (from point B to C) is reached. Such stress plateau indicates the Lüders deformation behavior, of which the first Lüders strain of $\approx 11\%$ tensile elongation is measured as the strain magnitude of the stress plateau on the engineering stress–strain curve. After such a stress plateau, a slight strain softening and hardening occurs, and is noticeably followed by the second Lüders band formation, which reaches a strain of 23.5%, corresponding to point D, and then disappears. When the second pass of the Lüders band is over, the ultimate tensile strength of 1020 MPa is shortly achieved at a strain of 28%. Afterward, necking occurs and is followed by a final failure.

The corresponding evolution of the 2D distribution of the strain rate during the tensile test at selected points in time, calculated on the basis of the DIC results, is illustrated in **Figure 4a**, while **Figure 4b** highlights the details of the Lüders band nucleation from a strain of 0.9% up to 1.65% sequentially in correspondence to **Figure 4a**. It has been observed from a strain level at point B (**Figure 3**), which corresponds to the lower-yield point at a strain of 0.9%, that a Lüders band nucleates first at the upper-right shoulder of the sample, and then develops across the gauge of the sample, showing $\alpha + 60^\circ$ angle to the tensile direction. After the band fully penetrates the width of the sample, a second band is initiated and develops through the first band, being inclined under -60° to the tensile direction. Hence, both overlapped bands form an X-shaped strain field in a localized

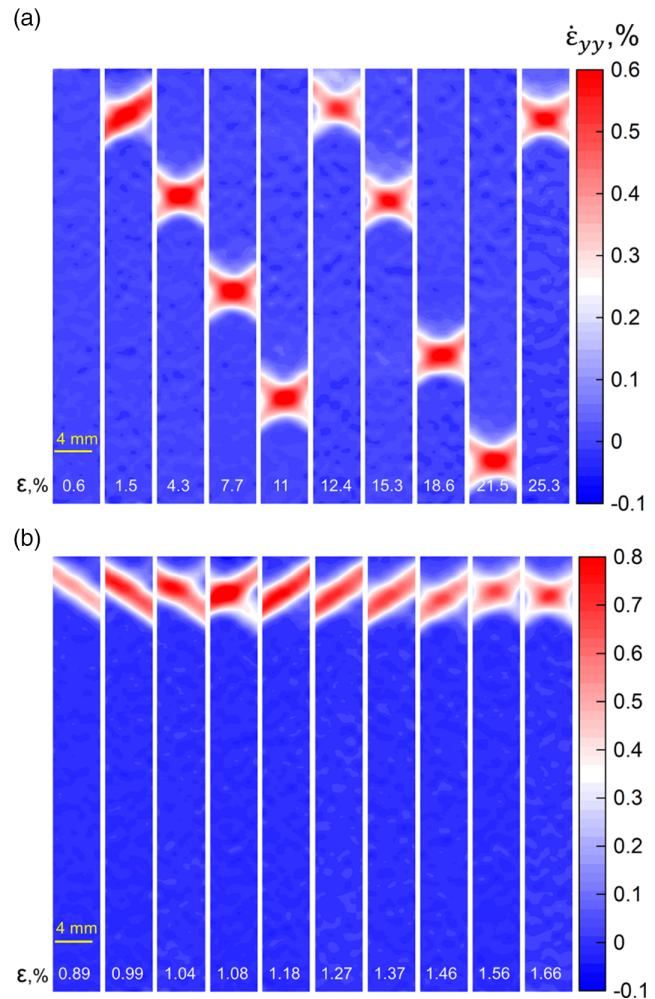


Figure 4. a) Ten strain-rate contour maps at the selected moments during the tensile test; b) a succession of strain-rate contour maps at the selected moments during the Lüders band nucleation.

region, which propagates continuously downward and eventually stops at point C as to be seen in **Figure 3**. By using a confocal microscope (Zeiss Smartproof 5), it can be observed, that the Lüders band (area C in **Figure 5**) does extrude, forming a protrusion with larger positive measured values than the undeformed area B. When continuing to apply tensile deformation, such bands further nucleate, almost at the same former position, and then propagated similarly from the upper to the lower end of the gauge section and are stopped in the end at a strain level corresponding to point D in **Figure 3**. After that, the X-shaped strain pattern shows up once again at the original position and stays saturated with necking until the final fracture. Such an observation suggests that the deformation-induced $\gamma \rightarrow \alpha'$ -martensite transformation, which promotes the enhancement of strength and ductility through the TRIP effect.

One of the microscopic models of the occurrence of Lüders band is related to the Cottrell atmosphere, the formation of atmospheres around dislocations, which was proposed by Cottrell and Bilby.^[28] It is postulated that the initial yielding

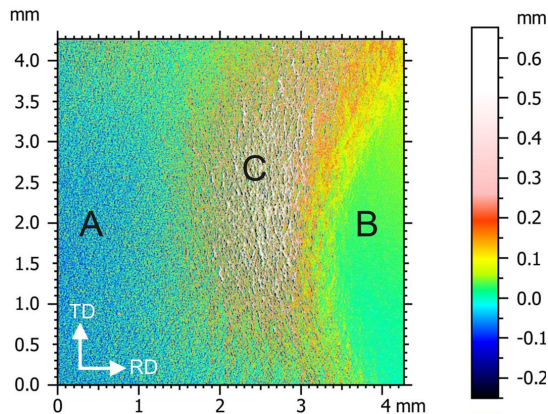


Figure 5. The 3D topography of the Lüders band and non-Lüders band areas within a $4.3 \times 4.3 \text{ mm}^2$ area at a strain of 7%. The image is acquired by a confocal microscope. A and B represents the deformed and undeformed areas, respectively, while C represents the Lüders band.

needs high stress for pulling out of those atmospheres and be once released, the dislocations can be moved by lower stress. However, it is reported that the Cottrell mechanism fails to explain the discontinuous yielding behavior in the current UFG medium Mn steel in recent years.^[29–31] With the help of advanced characterization technology, for example, atom probe tomography^[29] and in situ synchrotron high-energy X-Ray diffraction,^[29,30] it is investigated that grain morphology and interface chemical decoration have direct influence on the yielding phenomenon in this air-cooled medium Mn steel grade. The rapid dislocation nucleation at the austenite–ferrite phase boundaries is responsible for the discontinuous yielding. The Lüders band–governed elongation was explained in detail by Zhang,^[32] such as 1) strain softening: the plastic instability emerges instantly once yielding occurs due to the UFG microstructure’s low work-hardening ability. This behavior results in a reduction in the cross-sectional area of the sample, and then an abrupt drop happens at the yielding point. With the development of inhomogeneous strain, deformation will then be localized in a narrow band; 2) strain hardening: the TRIP effect

induced by inhomogeneous strain is a very effective way to display the work-hardening ability. Such strain hardening counteracts the plastic instability and further restrains localized deformation; 3) strain transfer: the inhomogeneous strain transfers from a hardened to an adjacent undeformed region, due to further localized deformation suppressed by the TRIP effect.

3.2. Variation in the Magnetic Barkhausen Noise

The variation in the curves of MBN signal intensities recorded versus coil voltage applied throughout the gauging zone is presented in **Figure 6a**. The measurement was undertaken with a cyclic magnetization along the same direction in the sample as the tension stress was applied. It can be noticed that the MBN intensity is highest in the unloaded condition, where no deformation has occurred. With increasing tensile deformation, the MBN signal intensity decreases as an overall trend. The variation of the MBN signal peak intensity and its peak position, where the peak position can be correlated to the coercivity of the material, were plotted together against the strain applied along the whole test procedure, as shown in **Figure 6b**.

It can be recognized that the 180° DWs grow at the expense of the 90° DWs during the elastic deformation, and thus the more obvious DW motion leads to the higher MBN response.^[19] The MBN signal intensity in the elastic regime decreases nearly linearly, this is attributed to the stress-sensitive feature of MBN, which results in the reduced peak height. In the plastic regime, as the deformation increases, the reduction continues, followed by a plateau until the end of the test. In the plastic instable stage until the first Lüders band initiation takes place, which corresponds to the region from point B to C in **Figure 3**, the change in MBN signal intensity is of special interest. From the upper-yield point to the valley of the σ - ϵ curve at a strain of $\approx 4\%$, the MBN peak value undergoes an irregular evolution, which may be caused by the stress relaxation of the compressive residual stress in the steel from the cold-rolling process.^[33] After that, the MBN peak value decreases continuously till the strain of 7.5% is reached and then fluctuates around $\approx 9.5 \times 10^3$. The fluctuation of the MBN signal intensity is likely to be related to the plastic flow during the tensile deformation, and the

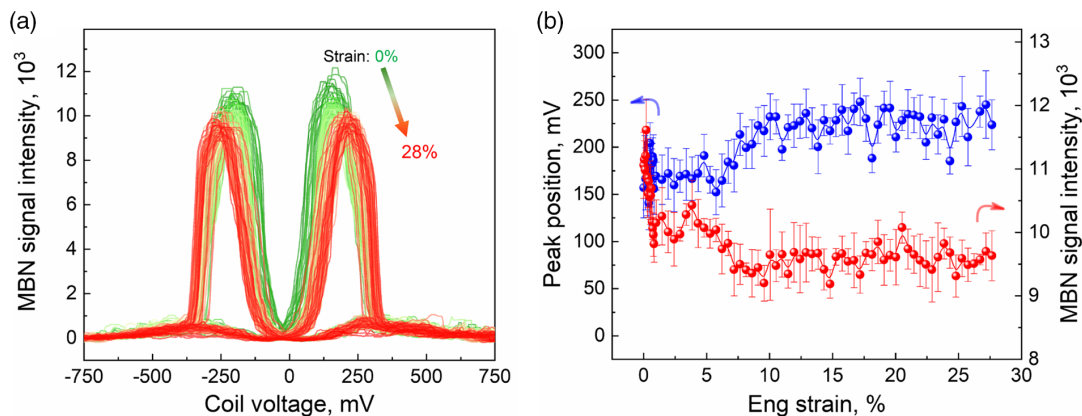


Figure 6. a) The magnetic Barkhausen noise (MBN) profiles measured at selected strains during the tensile test; b) the MBN signal intensity and peak position versus the tensile strain.

macroscopic phenomenon of the plastic flow observed can be correlated to the Lüders band propagation. The signal intensity of the MBN drops to a negligible value (not shown in Figure 6) at the point where the specimen reaches final fracture, since the local magnetization is interrupted.

The hardness of the material increases with the elongation due to the increased dislocation density caused by tensile deformation and the thereon related cold work processes, which impedes the dislocation motion and works to harden the material.^[33] The magnetic DWs can be held in place because of dislocation interactions or microstructural defects, so the magnetizing force is not strong enough to set the interactions free. Thus, the reduced DW motion will result in decreased Barkhausen activities.^[34] This phenomenon is called the “pinning” of DWs, which was proposed by Kittel^[35] and whose model takes the potential energy for the DW motion associated with the position to the potential obstacles, and further considers the inflexible wall whose motion is retarded by the defects density. If the defects are evenly distributed on both wall sides, then the force is zero, but otherwise, the force tends to move the wall to a more favorable position.^[19] The plastic deformation creates an increase in dislocation which acts as the pinning site to the DW motion, and further increases the potential wells for DW motion.^[36]

The increase in hardness of the medium Mn steel is due to the increase in pinning density for the magnetic DW motion and dislocation motion by the deformation-induced martensitic transformation (DIMIT) and the dislocation structures around the ferrite and martensite grains.^[33] With the increase in $\gamma \rightarrow \alpha'$ -martensitic transformation and the dislocation density during the tensile deformation, strong pinning for the magnetic DW motion will emerge to decrease the signal intensity of the MBN, which increases the coercivity of the material. When the magnetic field strength is fixed and higher than the maximum saturation level of the material even at a high deformation, the Barkhausen activity would be effected by the magnetic domains, and those domains will have enough energy to free them from the pinning sites. Thus, the increased plastic deformation results in the reduced DW motion, and which will,

in turn, reduce the Barkhausen activity at a fixed applied magnetic excitation field.^[19]

Magnetic materials with ultrafine grain normally reveal a high coercivity, because the high density of grain boundaries can provide more pinning sites for the DW motion.^[37] Additionally, as mentioned earlier, the magnetic coercivity is a physical quantity reflecting the dislocation density, which prevents the reversible magnetic domain rotation if the applied magnetic field is not strong enough to free them from the pinning sites. Thus, the increased dislocation density will result in an increased coercivity,^[38] that is, the coercivity can be used as a quantitative means to evaluate dislocation during tensile deformation of the medium Mn TRIP steel.

3.3. Microstructural Changes Along with the Tensile Deformation

The phase deformation and its resulting statistical analysis in terms of material characteristics can be supplied by XRD. The results for different states of the strain of the medium Mn steel are given in Figure 7. The fcc austenite phase shows the diffraction peaks of {111}, {200}, and {220}, while the bcc ferrite/bct martensite phases contribute the peaks of {110}, {200}, and {211}. As shown in Figure 7a, as a result of the increasing tensile strain, the intensity of austenite peaks is decreased ({111} and {220}) and has even disappeared ({200}), while the intensity of ferrite/martensite peaks is increased with increasing tensile deformation. The volume fraction of retained austenite- V_γ was determined from the XRD analysis and decreased to $\approx 9\%$ at the final fracture as given in Figure 7b, which indicates that a considerable portion of γ -austenite is transformed into α' -martensite. Hardness measurement with a load of 5 N and a holding time of 15 s was conducted on the samples using a Vickers hardness tester (Figure 7b). It becomes obvious that the hardness of the samples increased due to the martensitic phase transformation, and the increased dislocation density, as to be seen with the tensile deformation increasing from 370 HV in the annealed condition to 427 HV in the final fracture state.

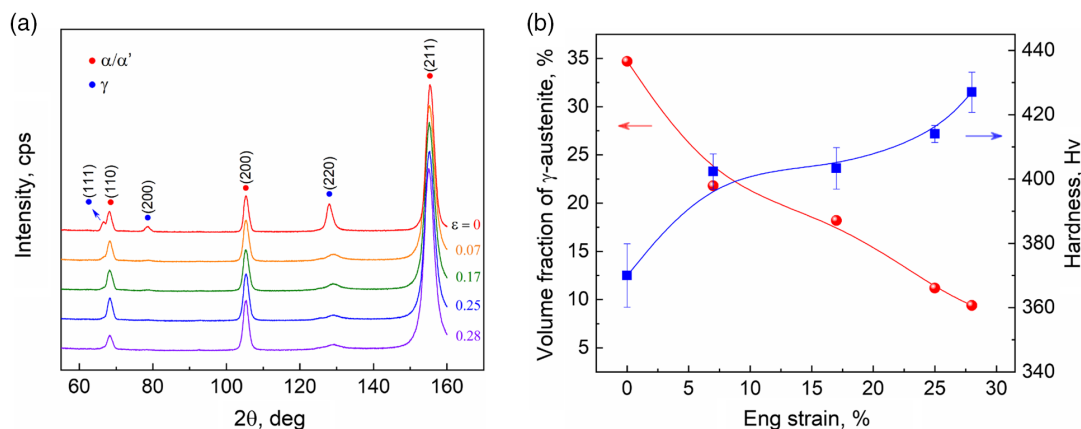


Figure 7. a) X-Ray diffraction (XRD) spectra measured at selected strains of the annealed samples; b) the transformation kinetics of retained γ -austenite measured from (a) and the corresponding statistical hardness of the samples.

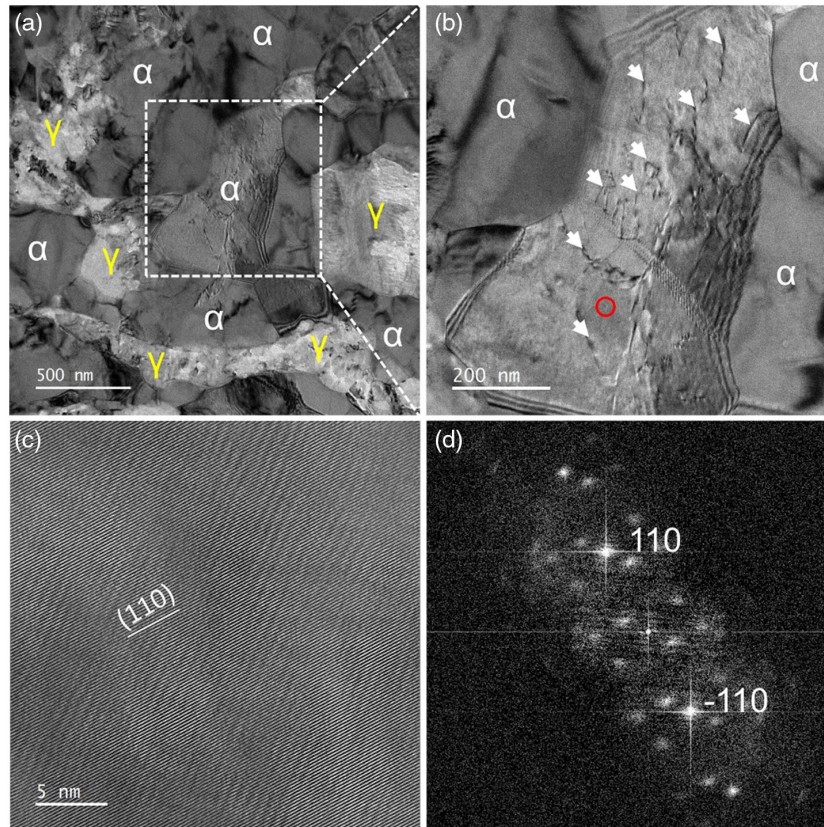


Figure 8. a) Transmission electron microscope (TEM) bright-field image of the annealed specimen before the tensile test. α : ferrite, γ : austenite. b) Magnified view of the white dashed rectangle marked in (a). The white arrows indicate the dislocations; c) high-resolution TEM image taken from the grain containing dislocations of the red circular region marked in (b); d) fast-Fourier transformation of the high-resolution TEM image.

The microstructure of the specimen before the tensile test observed by TEM is shown in **Figure 8a**, and enlarged in **Figure 8b**, showing the ROI marked in **Figure 8a**, which contains only a few grains. It is observed from the TEM images that the amount of dislocation contained in the microstructure is considerably low: a few dislocation lines emerge in the ferrite grain and barely appear in the neighboring grains. The dislocation density of the initial sample is $\approx 2.5 \times 10^{13} \text{ m}^{-2}$. Such a result is consistent with the annealing process. It is therefore ensured that the initial dislocation density in the annealed material is at a reasonably low level before the Lüders deformation is reached.

It should be noted that the martensitic transformation is not the cause of the Lüders band. Martensitic transformation and Lüders band generation are two independent mechanisms that happen simultaneously under certain applied stress conditions.^[25] The deformation-induced $\gamma \rightarrow \alpha'$ -martensite transformation normally results in a hard and brittle martensitic phase with high dislocation density and high density of geometrically necessary dislocations (GNDs) in adjacent ferrite grains.^[39] Then, the samples were individually analyzed using a TEM at different strain states, as shown in **Figure 9** for the phase with ongoing Lüders deformation ($\epsilon = 7\%$, 17% , 25%) as well as for the final fracture at 28% . It can be recognized from the microstructures that massive dislocations appeared in the deformed condition.

Comparison of **Figure 9** with **8** allows to conclude that the dislocation multiplications are on a very high level and lead to a high dislocation density generated during the Lüders band propagation. Thus, the reason why the deformation-induced $\gamma \rightarrow \alpha'$ -martensitic transformation plays a role in the hardness increase, as shown before in **Figure 7b**, is explained. The quantitative measurement of dislocations was conducted from the ROI of **Figure 8b** and **9a1–d1**, and the dislocation density versus the tensile deformation diagram is given in **Figure 10**, where both of the quantities are positively correlated, as discussed before. The dislocation density for the final fracture reached a very high value of $\approx 10^{14} \text{ m}^{-2}$. Thus, more and more magnetic DWs will get pinned or arrested in their position by the dislocation interactions and the magnetizing force is not high enough to set them free. Finally, the reduced domain motion will result in the decreased MBN.^[40]

In the high-level deformation, the high-density GNDs normally work as the obstacles to hinder the dislocation to slide in the ferrite grains and further provide the extra strain-hardening ability. Furthermore, the plastic deformation of the martensite with high dislocation density will also increase the strain-hardening ability.^[15] Such a behavior has a very close relation to the MBN activity and affects coercivity. Moreover, the deformation-induced $\gamma \rightarrow \alpha'$ -martensitic transformation provides a minor contribution to sustain the Lüders band propagation by

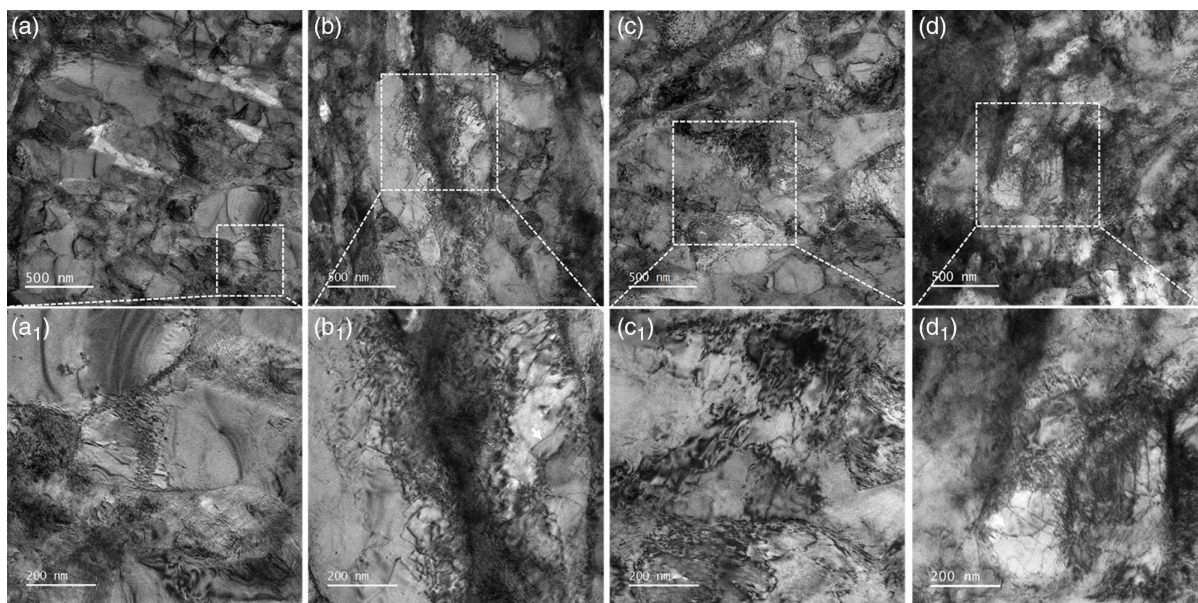


Figure 9. TEM images showing the evolution of the microstructures at the selected strains of a) 7%, b) 17%, c) 25%, and d) 28%, respectively.

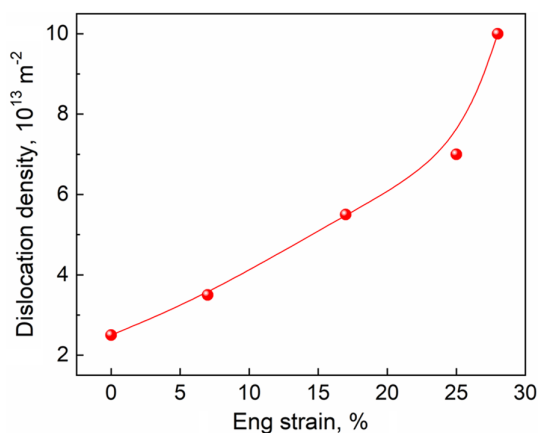


Figure 10. The equivalent dislocation density at selected strains of the annealed samples.

dislocation strength for the UFG medium Mn TRIP steel investigated here.

4. Conclusions

The mechanical and magnetic behavior of UFG medium Mn TRIP steel has been investigated and presented here with the following main conclusions to be made: 1) Nucleation and propagation of Lüders bands in plastic instability—at least for the TRIP steel presented here—can be visualized and possibly also further quantified by using DIC. The Lüders band-governed elongation can be correlated to the plastic instability, which includes strain softening, strain hardening, and strain transfer. 2) DIMT during plastic instability was analyzed applying a TEM, which indicates that a minor contribution of this sustains the Lüders band propagation by dislocation strength and affects

the deformation process of the Lüders band. 3) Phase content, hardness, and dislocation density of the samples at different selected strains, measured ex situ, allow the evolution of DIMT during tensile deformation roughly to be quantified. This affects the pinning sites of the DWs and can further help to understand the mechanical and magnetic behavior in the material exposed to tensile deformation. 4) DIMT behavior affects the MBN signal intensity and coercivity of the material. This nondestructive technique opens a wide range of possibilities to characterize and understand the deformation process in ferromagnetic materials, such as the UFG medium Mn TRIP steel.

Acknowledgements

Z.T. would like to acknowledge the support from the China Scholarship Council. The authors also thank the Carl-Zeiss-Stiftung for the funding of the Kerr microscope within the scope of the TELMa project. T. Bill and S. Raghuraman (HS-KL) are thanked for the technical assistance.

Open Access funding enabled and organized by Projekt DEAL.

Conflict of Interest

The authors declare no conflict of interest.

Data Availability Statement

The data that support the findings of this study are available from the corresponding author upon reasonable request.

Keywords

magnetic Barkhausen noise, medium manganese steel, plastic instability, transmission electron microscopy

Received: January 5, 2022
Revised: March 7, 2022
Published online: April 23, 2022

- [1] J. T. Benzing, A. K. da Silva, L. Morsdorf, J. Bentley, D. Ponge, A. Dutta, J. Han, J. R. McBride, B. Leer, B. Gault, D. Raabe, J. E. Wittig, *Acta Mater.* **2019**, 166, 512.
- [2] X. Tan, D. Ponge, W. Lu, Y. Xu, H. He, J. Yan, D. Wu, D. Raabe, *Acta Mater.* **2020**, 186, 374.
- [3] B. Sun, W. Krieger, M. Rohwerder, D. Ponge, D. Raabe, *Acta Mater.* **2020**, 183, 313.
- [4] B. Sun, D. Palanisamy, D. Ponge, B. Gault, F. Fazeli, C. Scott, S. Yue, D. Raabe, *Acta Mater.* **2019**, 164, 683.
- [5] X. G. Wang, L. Wang, M. X. Huang, *Acta Mater.* **2017**, 124, 17.
- [6] X. G. Wang, L. Wang, M. X. Huang, *Mater. Sci. Eng., A* **2016**, 674, 59.
- [7] H. Qiu, T. Inoue, R. Ueji, *Mater. Sci. Eng., A* **2020**, 790, 139756.
- [8] M. Zhang, L. Li, J. Ding, Q. Wu, Y. D. Wang, J. Almer, F. Guo, Y. Ren, *Acta Mater.* **2017**, 141, 294.
- [9] T. Kwok, K. M. Rahman, X. Xu, I. Bantounas, J. F. Kelleher, S. Dasari, T. Alam, R. Banerjee, D. Dye, *Mater. Sci. Eng., A* **2020**, 782, 139258.
- [10] S. Yan, T. Li, T. Liang, J. Chen, Y. Zhao, X. Liu, *Mater. Sci. Eng., A* **2019**, 758, 79.
- [11] J. T. Benzing, Y. Liu, X. Zhang, W. E. Luecke, J. E. Wittig, *Acta Mater.* **2019**, 177, 250.
- [12] J. J. Wang, W. J. Hui, Z. Q. Xie, *J. Mater. Sci.* **2020**, 55, 5296.
- [13] M. S. Jeong, T. M. Park, S. Choi, S. J. Lee, J. Han, *Scr. Mater.* **2021**, 190, 16.
- [14] B. C. De Cooman, P. Gibbs, S. Lee, D. K. Matlock, *Trans. A* **2013**, 44, 2563.
- [15] J. Ma, H. Liu, Q. Lu, Y. Zhong, L. Wang, Y. Shen, *Scr. Mater.* **2019**, 169, 1.
- [16] X. G. Wang, C. H. Liu, B. B. He, C. Jiang, M. X. Huang, *Mater. Sci. Eng., A* **2019**, 761, 138050.
- [17] Y. Ma, *Mater. Sci. Tech.* **2017**, 33, 1713.
- [18] Y. K. Lee, *Mater. Sci. Tech.* **2015**, 31, 843.
- [19] D. O'Sullivan, M. Cotterell, D. A. Tanner, I. Mészáros, *NDT&E Int* **2004**, 37, 489.
- [20] E. Hristoforou, A. Ktena, P. Vourna, K. Argiris, *AIP Adv.* **2018**, 8, 047201.
- [21] M. Lindgren, T. Lepisto, *NDT&E Int.* **2004**, 37, 403.
- [22] P. Haušild, K. Kolařík, M. Karlík, *Mater. Des.* **2013**, 44, 548.
- [23] D. O'Sullivan, M. Cotterell, I. Meszaros, *NDT&E Int.* **2004**, 37, 265.
- [24] P. B. Hirsch, *Electron Microscopy of Thin Crystals*, Butterworths, Oxford, UK **1965**.
- [25] X. G. Wang, B. B. He, C. H. Liu, C. Jiang, M. X. Huang, *Mater.* **2019**, 6, 100288.
- [26] B. Hu, H. Luo, *Acta Mater.* **2019**, 176, 250.
- [27] M. C. Somani, P. Juntunen, L. P. Karjalainen, R. D. K. Misra, A. Kyröläinen, *Metall. Mater. Trans. A* **2009**, 40, 729.
- [28] A. H. Cottrell, B. A. Bilby, *Proc. Phys. Soc.* **1949**, 62, 49.
- [29] Y. Ma, B. Sun, A. Schökel, W. Song, D. Ponge, D. Raabe, W. Bleck, *Acta Mater.* **2020**, 200, 389.
- [30] B. Sun, Y. Ma, N. Vanderesse, R. S. Varanasi, W. Song, P. Bocher, D. Ponge, D. Raabe, *Acta Mater.* **2019**, 178, 10.
- [31] K. Steineder, D. Krizan, R. Schneider, C. Béal, C. Sommitsch, *Acta Mater.* **2017**, 139, 39.
- [32] Y. Zhang, H. Ding, *Mater. Sci. Eng.* **2018**, 733, 220.
- [33] J. N. Mohapatra, A. K. Akela, *J. Nondestruct. Eval.* **2019**2019, 38, 22.
- [34] D. J. Buttle, C. B. Scruby, G. A. D. Briggs, E. A. Little, J. P. Jakubovics, *Phil. Trans. R Soc. Lond. A* **1986**, 320, 363.
- [35] C. Kittel, Galt J. K. Ferromagnetic Domain Theory, *Solid State Phys.* **1956**, 3, 437.
- [36] B. Astie, J. Degauque, J. L. Porteseil, R. Vergne, *J. Magnet. Magn. Mater.* **1982**, 28, 149.
- [37] J. S. Zhang, W. Li, X. F. Liao, H. Y. Yu, L. Z. Zhao, H. X. Zeng, D. R. Peng, Z. W. Liu, *J. Mater. Sci. Technol.* **2019**, 35, 1877.
- [38] R. A. Taylor, J. P. Jakubovics, *J. Magnet. Magn. Mater.* **1983**, 31–34, 970.
- [39] A. Ramazani, K. Mukherjee, A. Schwedt, P. Goravanchi, U. Prah, W. Bleck, *Inter. J. Plast.* **2013**, 43, 128.
- [40] D. O'Sullivan, M. Cotterell, S. Cassidy, D. A. Tanner, I. Mészáros, *J. Magn. Mang. Mater.* **2004**, 271, 381.